

JGR Space Physics

RESEARCH ARTICLE

10.1029/2020JA028774

Key Points:

- As the IMF B_z increases, mesoscale multiple quasistatic field-aligned currents embedded in the diminished dusk Region 1/2 become prominent
- The density of the mesoscale field-aligned currents tends to increase with the solar wind proton density
- The event appears regardless of whether the ionosphere is sunlit or dark

Correspondence to:

Y. Yokoyama,
yokoyama@kugi.kyoto-u.ac.jp

Citation:

Yokoyama, Y., Taguchi, S., & Iyemori, T. (2021). Importance of the northward IMF for the quasistatic mesoscale field-aligned currents embedded in the diminished Region 1/2 current system in the dusk sector. *Journal of Geophysical Research: Space Physics*, 126, e2020JA028774. <https://doi.org/10.1029/2020JA028774>

Received 1 OCT 2020
 Accepted 30 JUN 2021

Importance of the Northward IMF for the Quasistatic Mesoscale Field-Aligned Currents Embedded in the Diminished Region 1/2 Current System in the Dusk Sector

Y. Yokoyama¹ , S. Taguchi¹ , and T. Iyemori²

¹Department of Geophysics, Graduate School of Science, Kyoto University, Kyoto, Japan, ²Kyoto University, Kyoto, Japan

Abstract To understand the features of the quasistatic field-aligned currents (FACs) consisting of multiple mesoscale (~10–100 km) upward and downward FAC regions in the duskside auroral oval, we examined the magnetic field data obtained through the constellation measurements of Swarm satellites for a duration of more than three years. We introduced a method of automated event identification and took the events in 577 satellite orbits that pass through the high-latitude part of the 14–18 magnetic local time auroral oval. The results of the analysis reveal that the occurrence ratio of the FAC events increases with the IMF B_z , and that the event can be detected at a ratio exceeding 20% for B_z greater than 1 nT. This indicates that the quasistatic mesoscale FACs in the duskside sector are pertinent to a northward IMF condition and that they are not a simple remnant of the diminished Region 1. The results also show that the FAC density tends to increase with the solar wind proton density, implying that the latter is directly associated with FAC generation. The FAC events can occur in a wide range of solar zenith angles, that is, 65–135°, indicating that whether the ionosphere is sunlit or dark is not crucial for the appearance of the event. These results strongly suggest that multiple mesoscale FACs are produced in the low-latitude boundary layer through a mechanism related to solar wind plasma entry processes that can be more easily attained as the northward component of the IMF increases.

1. Introduction

The magnetic perturbations observed by low-altitude polar-orbital spacecraft generally exhibit prominent large-scale deviations in the east-west direction in the auroral zone. These deviations are caused by the quasistatic Region 1/2 field-aligned current (FAC) system flowing away from or into the polar ionosphere. The smaller scale magnetic variations include both those produced by the quasistatic FACs and the dynamic FACs (typically Alfvén waves), which fluctuate over time. Multisatellite observations are beneficial toward determining the extent to which magnetic perturbations are produced by Alfvén waves or the quasistatic structure of FACs (Gjerloev et al., 2011; Lühr et al., 2015). The magnetic perturbations having horizontal scale sizes of down to 150–200 km can be regarded as being caused by the quasistatic FACs, while the magnetic perturbations having horizontal scale sizes of up to approximately 10 km can be ascribed to the Alfvén waves. It appears that the perturbations having horizontal scale sizes between them are caused by both FACs.

A recent study by Yokoyama et al. (2020) examined magnetic field data from multiple Swarm satellites (Fris-Christensen et al., 2006), which were shown by the above-mentioned earlier study (Lühr et al., 2015) to be effective for the identification of the quasistatic FAC structures, in combination with aurora data from a ground-based all-sky imager (Taguchi et al., 2012). Yokoyama et al. (2020) found that the duskside mesoscale FACs with latitudinal sizes of 20–30 km, which were prominent for the northward IMF, were quasi-persistent. This type of mesoscale FACs was identified as a phenomenon for prolonged geomagnetic quiet time over 30 years ago (Rich & Gussenhoven, 1987); however, where those FACs were generated has been unclear for a long time. Yokoyama et al. (2020) also used precipitating particle and magnetic field data from the Defense Meteorological Satellite Program (DMSP) spacecraft, together with the data from the all-sky imager, and suggested that mesoscale FACs that were prominent for the northward IMF were generated in

multiple embedded parts in the low-latitude boundary layer (LLBL), wherein the cold dense ions originating from the magnetosheath decelerated.

The existence of cold dense ions in the LLBL during the prolonged northward IMF period was revealed by in situ observations by the Geotail satellite (Fujimoto et al., 1998; Terasawa et al., 1997). Subsequent studies on the mechanism of their existence have indicated that the plasma motion associated with the Kelvin–Helmholtz (KH) instability plays a significant role in the existence of cold dense ions (Fairfield et al., 2000; Hasegawa, Fujimoto, Phan, et al., 2004; Otto & Fairfield, 2000). When we consider that the cold dense ions are a result of the plasma motion from the magnetosheath to the magnetosphere, it may be reasonable that FACs flow away or into the region of the cold dense ions because the plasma motion in the magnetosphere can generally produce FACs. However, further studies are required to understand how important the cold dense ion region in the LLBL is for the formation of mesoscale FACs in the dusk sector for the northward IMF. This is because the two events that have been examined by Yokoyama et al. (2020) have both been from the low conductivity ionosphere and it is unclear if low conductivity is an important condition for the appearance of mesoscale FACs. When mesoscale electron precipitation occurs under the background of the lower conductivity ionosphere, the spatial gradient of the conductivity would be larger, which might produce FACs. However, if the low conductivity condition is not crucial for the occurrence of mesoscale FACs, the specific solar wind conditions essential for FAC generation need to be understood.

In this study, by collecting a large number of mesoscale FAC events in the duskside sector, we understand the above-mentioned questions through their statistical properties. As shown in the study of Yokoyama et al., 2020 (their Figure 6b), mesoscale FACs can be found in the high latitude part of the auroral oval. We applied a method of automated event identification to the magnetic field data obtained by multiple Swarm satellites traversing the high latitude part of the duskside auroral oval.

2. Data

The Swarm constellation mission consists of three identical near-polar orbiting satellites A, B, and C, launched on November 22, 2013 by the European Space Agency (ESA). Each of the three satellites carries the fluxgate magnetometer and measures the magnetic field vector (Friis-Christensen et al., 2006). In this study, we subtracted the International Geomagnetic Reference Field (IGRF-12, Thébault et al., 2015) from the coordinate converted magnetic field vector in the North-East-Center local Cartesian coordinates (Olsen et al., 2013), whose resolution is 1 Hz, and we analyzed the east-west component of the magnetic perturbations.

Among the three satellites, SW-A and SW-C have been flying side-by-side, separated by 1.4° in longitude at an altitude of approximately 460 km with a slight time difference (approximately 10 s) since April 17, 2014 (SW-C ahead of SW-A). This satellite configuration helps us to understand whether FACs, which cause magnetic perturbations, are stable during such a short time period. In this study, we analyzed the data obtained in the northern hemisphere by SW-A and SW-C during the period from May 2014 to May 2017. We also used current density data, which are available as Swarm Level 2 products. The ESA provides two types of current densities, which is calculated using a single spacecraft solution and a dual spacecraft solution (Ritter et al., 2013). We used the former data in this study. For solar wind and IMF, we used the OMNI 1-min data.

3. Analysis

3.1. Method for the Event Identification

We required the following four conditions for automated event identification: (1) SW-A and SW-C traversed the high-latitude part of the duskside auroral oval; (2) the collocated large-scale Region 1/2 systems are diminished, and the magnetic perturbations produced by the mesoscale FACs are larger than those produced by the diminished large-scale Region 1/2 system; (3) the mesoscale FACs consist of multiple (at least five upward/downward current) regions; and (4) the mesoscale FACs show quasistatic features.

For Condition 1, we determined the “duskside” range as 14–18 magnetic local time (MLT), as adopted by Yokoyama et al. (2020). The boundary of 14 MLT was chosen so that the cusp FACs could be excluded

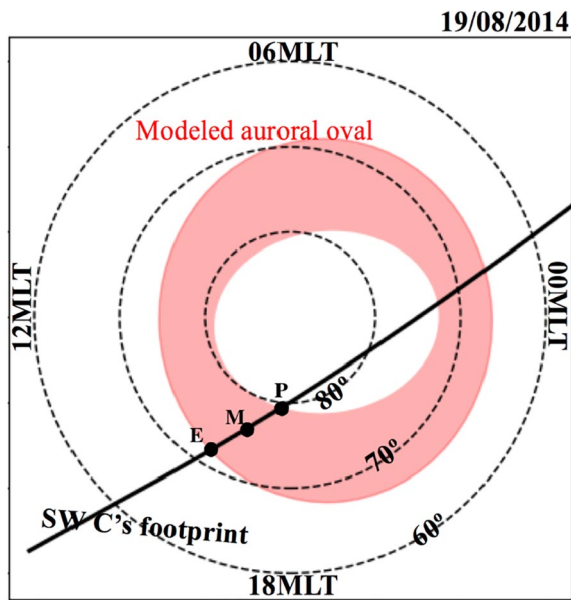


Figure 1. One of the SW-C passes on the MLT-MLAT dial (solid black line) in the magnetic apex coordinates, and corresponding auroral oval (shaded red region), which was calculated from the model by Xiong and Lühr (2014). The point *E* (or *P*) represents the intersection of the orbit and the equatorward (or poleward) boundary of the duskside part of the auroral oval, and *M* is the middle of their points. For this pass on August 19, 2014, *E* corresponds to the SW-C position at 13:36:06 UT. The actual SW-C data will be shown in Figure 3.

(Taguchi et al., 1993; Wing et al., 2010). Because the orbits of SW-A and SW-C are not exactly parallel to the MLT meridian, we apply slightly different conditions only to the orbits crossing the 14 MLT and 18 MLT boundaries, as shown below.

To determine the “high latitude part” of the auroral oval for each pass, we used the empirical auroral oval model developed by Xiong and Lühr (2014). This empirical model gives the poleward and equatorward boundaries of the auroral oval for the input of the 3-h time series of the IMF B_Y , B_Z , and the solar wind velocity. In Figure 1, we show an example of the auroral oval model together with one of the SW-C orbits. The black line indicates the SW-C orbit, while the black dot shown as *E* (or *P*) on the line represents the intersection of that orbit and the equatorward (or poleward) boundary of the model auroral oval. The black dot *M* is the middle of these two points. In the 3-h time series for the model input, we used the data of IMF B_Y , B_Z , and the solar wind velocity starting from $t = (t_0 - 3.5)$ h to $(t_0 - 0.5)$ h, considering a 30-min time delay, where t_0 is UT when SW-C crosses 70 magnetic latitude (MLAT). The 30-min delay is consistent with the result by Xiong and Lühr (2014). We also note that the model by Xiong and Lühr gives fixed boundaries irrespective of the IMF B_Z and the solar wind velocity if IMF is purely northward ($B_Y = 0$).

For each SW-C duskside pass, we calculated the location of *E*, *M*, and *P* by using the model and determined the range between *M* and *P* as the high latitude part of the auroral oval. It is required that both *M* and *P* should be within 14–18 MLT. In other words, we acknowledged that *E* may not be necessarily within this MLT range. The actual inputs (3-h, i.e., 180 OMNI data points) for the calculation of the auroral oval shown in Figure 1 will be subsequently discussed. We calculated the auroral oval model as far as the missing OMNI data points were less than 60. We then obtained 4,099 passes that satisfied Condition 1.

Next, for the passes that satisfied Condition 1, we analyzed the magnetic perturbation data along each pass. We linearly detrended the magnetic perturbations over the range between *E* and *P*, and then applied a low-pass filter with a cutoff period of 50 s to the linearly detrended data. With this filter we intended to extract the generally eastward magnetic variations whose spatial length is approximately 200 km, that is, roughly half of 7.8 km s^{-1} (satellite velocity) \times 50 s. The typical Region 1/2 magnetic variations, which are generally eastward, have such a spatial length (e.g., Gjerloev et al., 2011; Iijima & Potemra, 1978). We regarded the filtered data as large-scale Region 1/Region 2 variations, and the difference between the original data and the low-pass filtered data as the mesoscale variations. We note that even if the latitudinal scale length of the Region 1/2 is longer than 200 km (e.g., Huang et al., 2017), those variations will be extracted with that low-pass filter. We also note that the locations of the local maxima of the mesoscale variations do not agree with those of the FAC densities.

We also determined the “amplitude” of the large-scale variations as half of the difference between the maximum and minimum values of the filtered data so that we could estimate the magnitude of the large-scale variations without determining the baseline of the low-pass filtered data. For the mesoscale variations, we considered the maximum perturbation for each pass. Then, we included orbits wherein the maximum perturbation of the mesoscale variations is larger than the “amplitude” of the large-scale variations, that is, orbits in which the mesoscale FACs are prominent (Condition 2).

For the condition of the multiple current regions (Condition 3), we first considered the local maxima and minima from the mesoscale variations between *E* and *P*, and then defined each upward/downward FAC region as the region between the point for one local maximum and that for one local minimum. We also calculated the current intensity of each FAC region (unit of A m^{-1}) from the value of the difference between the local maximum and local minimum. For this calculation, we used the original magnetic perturbations

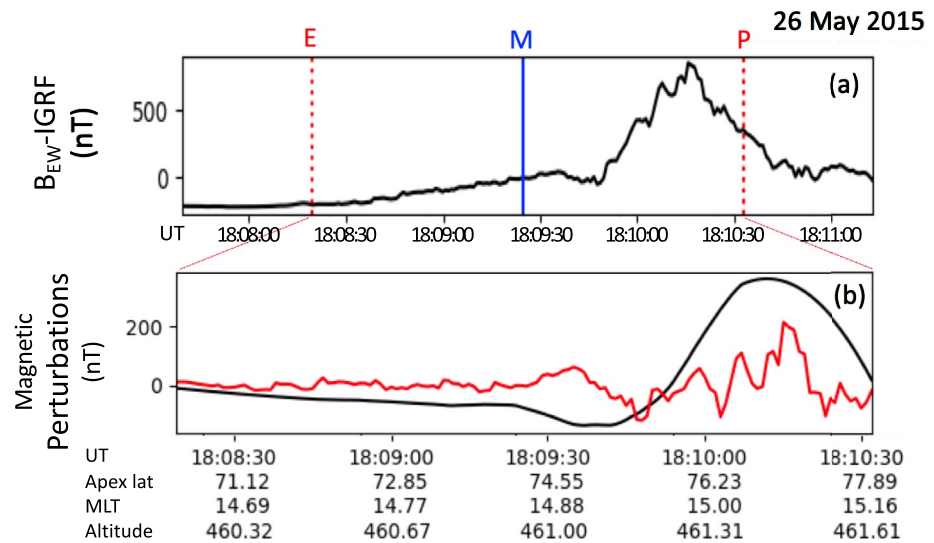


Figure 2. (a) Magnetic perturbations (east-west component) observed by SW-C during 18:07:39 UT–18:11:12 UT on May 26, 2015, (b) Expanded plots of the mesoscale (red) and large-scale (black) magnetic variations for 18:08:19–18:10:32 UT.

rather than the mesoscale variations to more accurately evaluate the current intensity because the mesoscale variations were somewhat smoothed out due to filtering effect, and artificial small perturbations were added. We considered the passes where five or more mesoscale current regions could be determined with the condition that the region with a current intensity of less than 20% of the maximum current intensity for each pass is ruled out.

For Condition 4, we employed the method used by Yokoyama et al. (2020). We used 30 data points (=30 s) around a given time for each of the SW-C data and SW-A datasets, and moved the SW-A data window by 1 s. As shown in Yokoyama et al. (2020), the correlation between the SW-A data shifted by the satellite separation time (usually 3–10 s) and the SW-C data should be high in the region where quasistatic FACs existed. We compared the SW-A data that were shifted by the satellite separation time and the SW-C data, and obtained the correlation coefficient in each 30 s window for the range between *M* and *P* points of SW-C. When the average of the correlation coefficients was higher than 0.6, we regarded the mesoscale magnetic variations as being quasistatic. We found events of quasistatic mesoscale FACs embedded in the diminished Region 1/2 current system in 577 passes out of the 4,099 passes.

3.2. An Example of the Events

Before showing an example of the quasistatic mesoscale FACs embedded in the diminished Region 1/2 current system, we show an event wherein the large-scale Region 1/2 current system develops well and the mesoscale magnetic variations are not remarkable. Figure 2a shows the east-west component of SW-C magnetic perturbation data for that event, that is, 18:07:39 UT to 18:11:12 UT on May 26, 2015. In this case, points *E* and *P*, which were derived from the auroral oval model, are (70.48° MLAT, 14.66 MLT) and (77.99° MLAT, 15.18 MLT). The locations of these points are shown with the two vertical red dotted lines (at 18:08:19 and 18:10:32 UT) in Figure 2a. The blue vertical line in Figure 2a represents the location of *M*. The positive and negative gradients of the magnetic perturbations represent FACs flowing into and away from the ionosphere, respectively. It is evident that the dominant parts of Region 1 flowing away from the ionosphere and Region 2 into the ionosphere occur between *E* and *P*.

Figure 2b shows a comparison between the large-scale variations (solid black line) and the mesoscale variations (solid red line). The “amplitude” of the large-scale variations is 250.3 nT, while the maximum of the mesoscale variations is 214.2 nT. Because the latter is smaller than the former, Condition 2 of our method does not regard this observation as an event of mesoscale FACs.

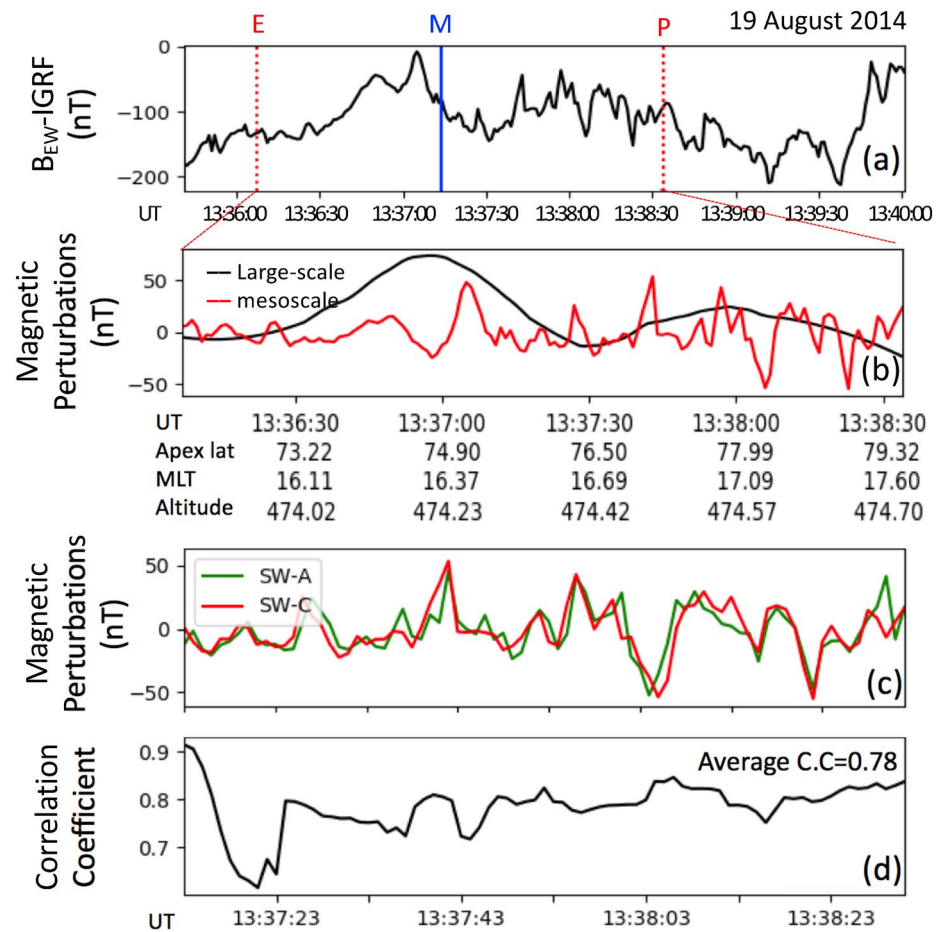


Figure 3. (a) Magnetic perturbations (east-west component) observed by SW-C during 13:35:46 UT–13:40:02 UT on August 19, 2014, (b) Expanded plots of the mesoscale (red) and large-scale (black) magnetic perturbations for 13:36:06–13:38:32 UT, (c) Comparison plot wherein the 6 s shifted SW-A data (green) are superposed on the SW-C data (red) between *M* and *P*, and (d) Plot of the correlation coefficients in each 30 s window between the SW-A and SW-C data.

In Figure 3, we show an example of the quasistatic mesoscale FACs. This event occurred on August 19, 2014. The points *E* and *P* for this event are (71.84° MLAT, 15.93 MLT) and (79.40° MLAT, 17.63 MLT). SW-C was in *E* and *P* at 13:36:06 UT and 13:38:42 UT, respectively. Figure 3a shows the east–west component of magnetic perturbations observed by SW-C from 13:35:46 UT to 13:40:02 UT.

A comparison plot between the large-scale and mesoscale variations is shown in Figure 3b. The “amplitude” of the large-scale variations is 44.1 nT, while that of the mesoscale variations is 57.9 nT. These values satisfy the aforementioned Condition 2. It is evident from Figures 3a and 3b that the highly structured magnetic perturbations are prominent at higher latitudes. The positive and negative gradients of the magnetic perturbations indicate FACs flowing into and away from the ionosphere, respectively. Multiple mesoscale FAC regions were observed. The large-scale variations (black line in Figure 3b) increased very gradually from the beginning of the plot, reached a maximum at ~13:37:00 UT, and then gradually decreased. This type of variation is consistent with the existence of large-scale Region 1/2 currents.

Figure 3a also shows that a sharp positive gradient starts at approximately 13:39:40 UT. This point is well poleward of *P*. The positive gradient represents the FAC flowing into the ionosphere, that is, a part of the duskside cell of the dayside polar cap FACs typical of the northward IMF condition (Araki et al., 1984; Carter et al., 2020; Iijima et al., 1984; Taguchi et al., 2015; Vennerstrøm et al., 2002). We note that this type of FAC is properly excluded in the present analysis by introducing the poleward boundary of the auroral oval, that is, *P*.

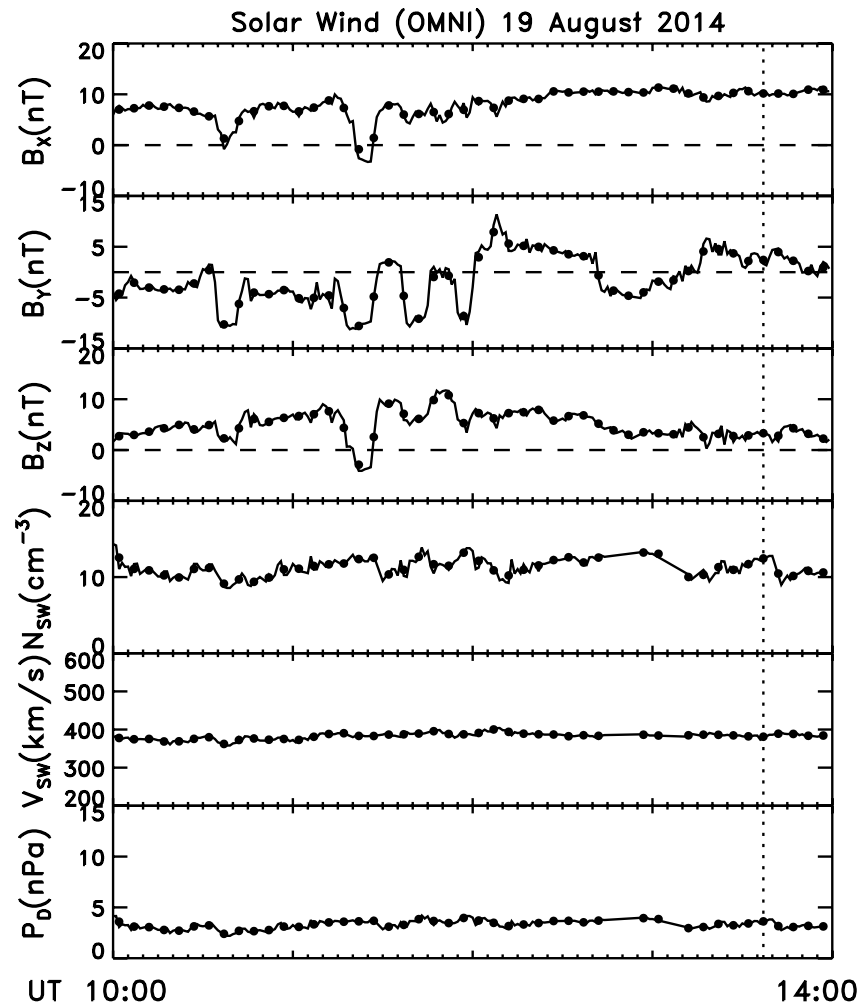


Figure 4. Solar wind and IMF data from OMNI between 10:00 UT and 14:00 UT on August 19, 2014. From top to bottom, the three components of IMF (B_x , B_y , and B_z) in GSM coordinate, the solar wind proton density, the flow speed, and the dynamic pressure are plotted. The vertical dotted lines at 13:37:13 UT indicate the time when SW-C crossed the point M of the modeled auroral oval, which is shown in Figure 1.

Figures 3c and 3d show the comparison in the region between M and P . In Figure 3c, we superpose the 6 s (separation time of the satellites) shifted SW-A data (green) on the SW-C data (red); these two data lines overlap very well. Evidently, dominant mesoscale variations are produced by quasistatic FACs. The plot in Figure 3d is the correlation coefficient, which shows that the correlation coefficient generally exceeds 0.7. The average for the range between M and P was 0.78.

Figure 4 illustrates the solar wind and IMF data for the event shown in Figure 3. We used the solar wind and IMF data both for the input for the aforementioned auroral oval model and for the statistical analysis on the occurrence characteristics, which will be subsequently shown. The solid line and dots in each panel of Figure 4 indicate 1 and 5 min OMNI data, respectively. From top to bottom, the three components of IMF (B_x , B_y , and B_z) in the geocentric solar magnetospheric system (GSM) coordinates, solar wind proton density, flow speed, and dynamic pressure are plotted. The vertical dotted line at 13:37:13 UT indicates the time when SW-C crossed the point M of the corresponding auroral oval model (Figure 1).

The IMF B_x (top panel) and B_z (third panel) were continuously positive throughout this duration except for 11:21–11:26 UT. During ~ 30 min before the time shown with the vertical dotted line, B_x and B_z were approximately constant, and their averages were 10.1 and 3.2 nT, respectively. B_y (second panel) had been positive for approximately 20 min since 13:15 UT. The 30-min average of B_y is 2.6 nT. The solar wind proton

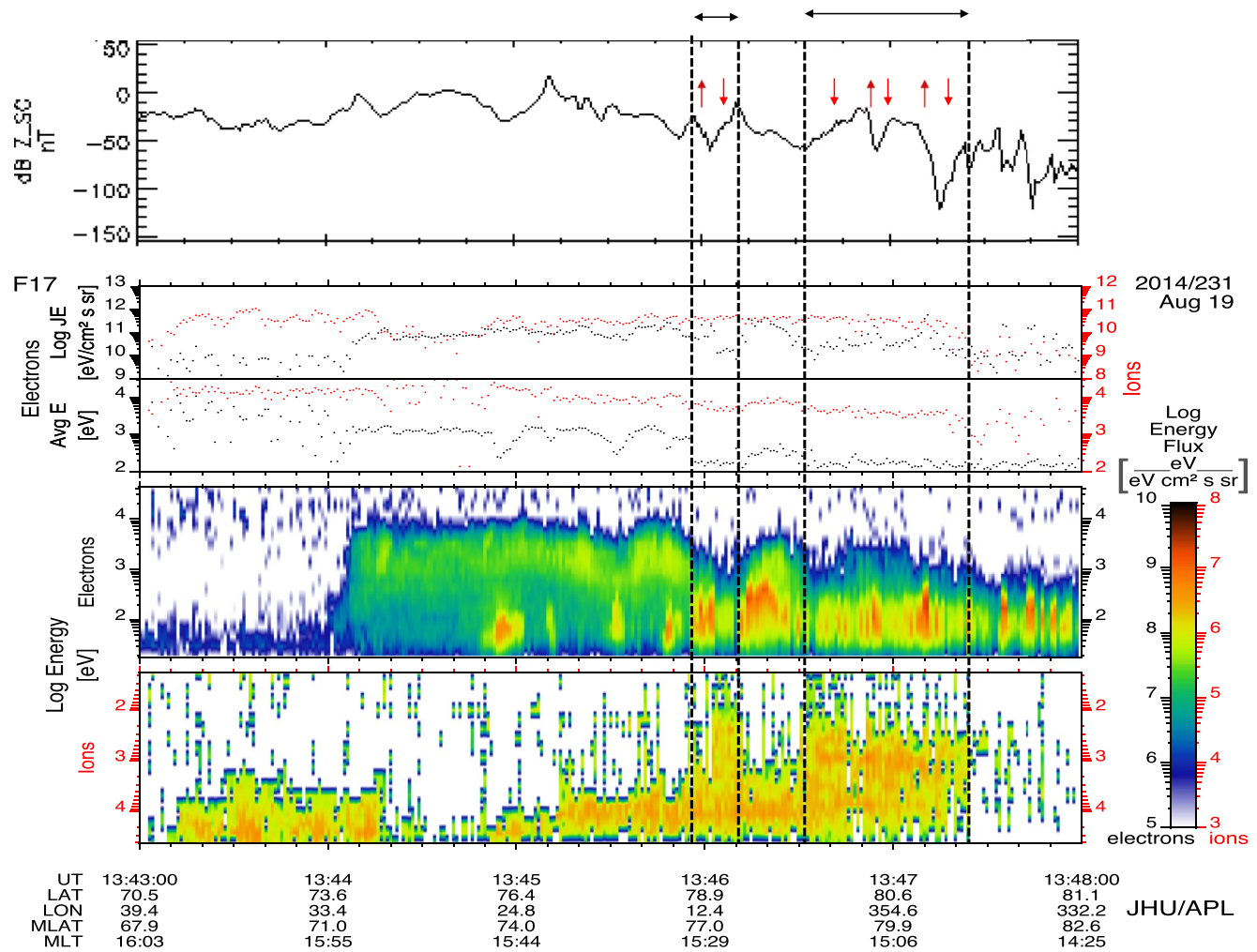


Figure 5. DMSF F17 data from magnetic field experiments and particle spectrometer during 13:43:00 to 13:48:00 UT. The top panel shows the Z component of the baseline-corrected magnetic field perturbation data in the spacecraft coordinates. In the bottom, the energy fluxes of the electrons and ions are plotted with color codes, together with the integral energy flux and average energy of the electrons and ions. Note that the ion energy axis is inverted in the fifth panel.

density, speed, and dynamic pressure were very stable throughout this period, and their 30-min averages were 11.1 cm^{-3} , 384 km s^{-1} , and 3.3 nPa , respectively. We used these 30-min average values for statistical analyses. This is consistent with our earlier result from the event study, which shows that the mesoscale FAC structures are stable during at least approximately 30 min (Yokoyama et al., 2020).

Figure 5 shows the data from the DMSF F17 magnetic field experiments and particle spectrometer from 13:43:00 to 13:48:00 UT. In this observation, DMSF passed through the similar MLT meridian to that of the SW-A/C event shown in Figure 3 (or Figure 1) immediately ~ 5 min after the passage of SW-C through point *P*. From top to bottom of Figure 5, the Z component of the baseline-corrected magnetic field perturbation data in the spacecraft coordinates, the integral energy flux and average energy of the electrons and ions, and the energy flux of electrons and ions with color codes are shown. The Z component is perpendicular to both the local vertical direction and the forward direction of travel, and thus it can be regarded as almost the same component as the Swarm east-west component in the auroral oval. The ion data show that DMSF observed the region of relatively low-energy ion precipitation (down to a few hundred electron volts) twice, that is, from 13:45:56 to 13:46:11 UT and 13:46:32 to 13:47:24 UT (vertical dotted lines). Low-energy electron precipitation is also prominent in these regions (fourth panel). As is also evident in the third panel (black dotted line), the average energy of the electron precipitation in these regions is generally lower than 200 eV. The top panel of Figure 5 shows that mesoscale magnetic perturbations, that is, mesoscale FACs, occur in

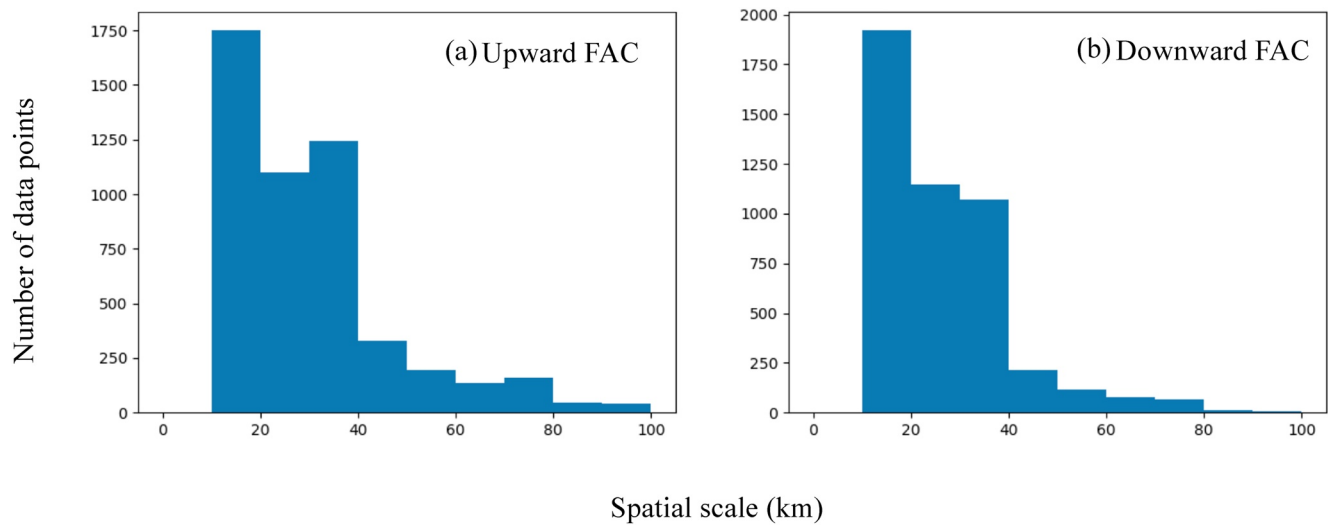


Figure 6. Distribution of the latitudinal size of the (a) upward FAC and (b) downward FAC observed by SW-C.

these regions. Thus, these DMSP observations imply that multiple mesoscale FACs occur along the field lines connected to the LLBL where cold ions exist. Consequently, it seems that the mesoscale FACs observed by SW-A/C (shown in Figure 3) also flow along the field lines connected to the LLBL.

3.3. Statistical Results

3.3.1. Latitudinal Size

The mesoscale duskside FAC event consists of multiple upward and downward FAC regions, as shown in Figure 3. We analyzed the magnetic field perturbations from the 577 passes and examined the latitudinal size (≥ 10 km) of the upward and downward FAC region. For each pass, we searched for two or more consecutive points with the same current polarity from the region between M and P , and took the period of the upward/downward current. We used current density data available as Swarm Level 2 products for this analysis (also for the analysis for Figures 9 and 10, which are shown later). To obtain the latitudinal size, we multiplied the period of each upward/downward FAC region by satellite velocity (7.8 km s^{-1}) and $\cos \alpha$, where α is the acute angle between the direction of the satellite orbit at the satellite's entry of each upward/downward FAC region and the MLT meridian. If α is zero, the latitudinal size is estimated to be one of the following: 15.6, 23.4, 31.2, 39.0, 46.8, 54.6 km.

Figures 6a and 6b show the distributions of the latitudinal size of the upward and downward FAC regions, respectively. The small-scale magnetic perturbations (up to about 10 km) tend to be caused by the Alfvén wave (Lühr et al., 2015). Since each event contains multiple upward/downward FAC regions, the number of data points (the ordinate of the histograms in Figures 6a and 6b) are much larger than the number of the event, that is, 577. The distributions in Figures 6a and 6b have a tendency to show that the latitudinal size does not usually exceed 40 km. This generally agrees with our earlier result from the event study, which shows that the typical latitudinal size of the mesoscale upward FACs is 20–30 km (Yokoyama et al., 2020).

3.3.2. Relation to the Solar Zenith Angle

The two events examined by Yokoyama et al. (2020) were from the winter season, that is, those obtained in the dark ionosphere. This was simply because they focused on the simultaneous observations from the satellites and the all-sky auroral imager, which was operative for the dark ionosphere. We here examine whether this is a distinct feature of the dark ionosphere or otherwise.

Figure 7 shows the histogram of the solar zenith angles of the 577 events, and the occurrence ratio of those events in each 10° bin of the solar zenith angle. The SW-C passes (4,099 in total) were divided into 10° bins by using the value of the solar zenith angle at each SW-C middle point between P and M . The number in

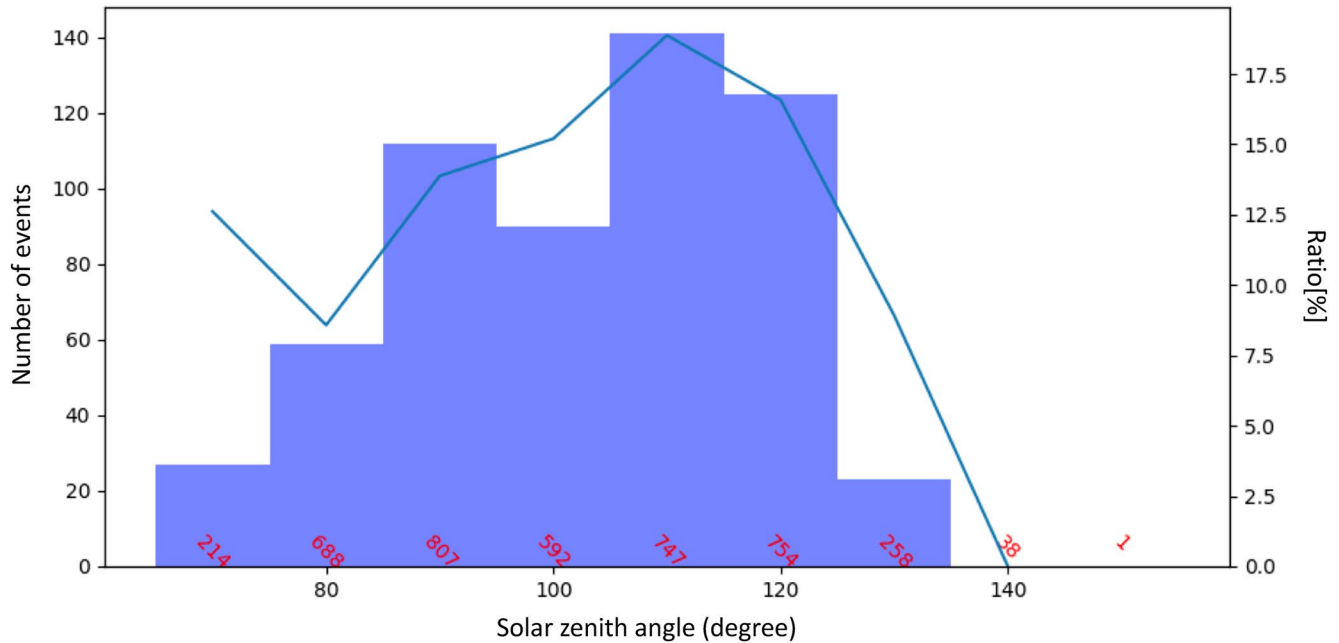


Figure 7. Histogram of the occurrence number of events (blue bars), and the occurrence ratio (light-blue line) as a function of the solar zenith angle.

each bin is shown in red at the bottom of Figure 7. The bar shown in blue indicates the number of events in each bin, while the line plot is the occurrence ratio.

The events can occur under a wide range of solar zenith angles from 65 to 135°, although the occurrence ratio is rather high at solar zenith angles between 105 and 125°. This result suggests that the low ionospheric conductivity, which occurs for larger solar zenith angles, that is, in the dark ionosphere, does not play an important role in the generation of the duskside multiple mesoscale FACs. The case of higher ratios for the dark ionosphere will be briefly discussed in Section 4.3.

3.3.3. Relation to the Solar Wind Parameters

Figures 8a–8c show the relation to the three components of the IMF. We used the IMF values averaged for 30 min immediately before the SW-C entry to M , as stated in Section 3.2. We calculated the averages as far as missing data points in the 1-min OMNI data do not exceed 10. In Figures 8a–8c the number of the events and the occurrence ratio are shown with 1 nT bin width. The occurrence ratio (light-blue line) is not shown for the bins, where the number of passes is very small (not exceeding 15 passes).

A notable tendency can be seen in the relation to IMF B_z (Figure 8c). The occurrence ratio of the FAC events is less than 10% for IMF B_z of <-1 nT, and as B_z increases, the occurrence ratio becomes high. For B_z greater than 2 nT, the event can be detected at a ratio of more than 20%. This shows that the quasistatic mesoscale FAC in the duskside sector is a phenomenon that is pertinent to the northward IMF condition, and not a simple remnant of Region 1. For B_x and B_y , no clear dependence is evident.

3.3.4. Current Density

We also examined whether there were any solar wind parameters that affected the current density of the FACs. For this examination, we first searched for two or more consecutive points with the same current polarity from the region between M and P for each SW-C pass, as was done for the analysis of the latitudinal size (Figure 6), and obtained the current density in the respective region. Collecting those upward and downward current densities from each pass separately, we then obtained the average upward/downward current density for each event.

Figures 9a–9d show the scatter plot of the current density of the FACs as a function of three solar wind plasma parameters and IMF B_z . Note that the vertical axis of these plots is inverted such that the negative current density, which is antiparallel to the earth magnetic field in the northern ionosphere, can be shown

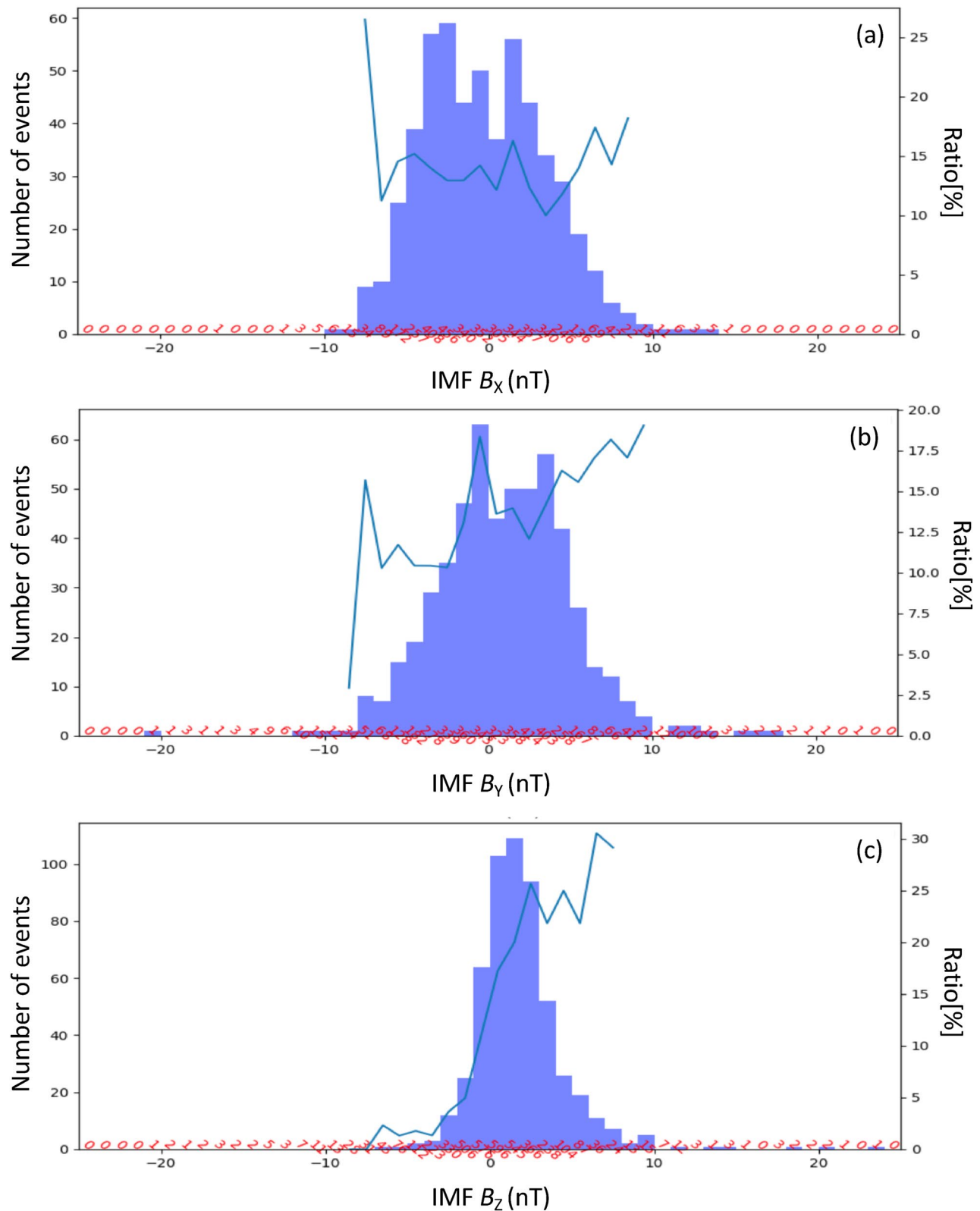


Figure 8. Histogram of the occurrence number of events (blue bars), and the occurrence ratio (light-blue line) as a function of three components of IMF: X, Y, and Z components from top to bottom, respectively.

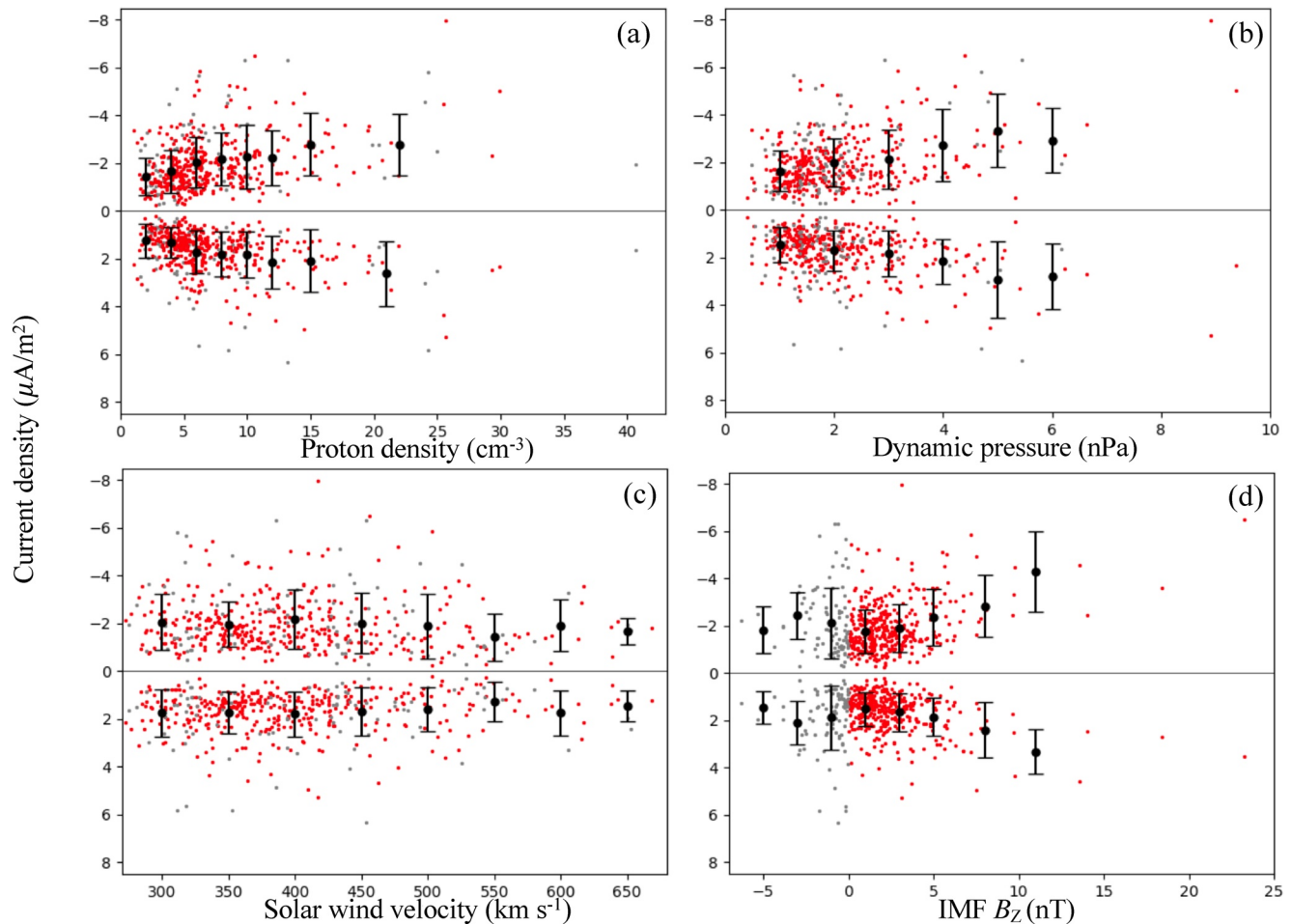


Figure 9. Scatter plot of the current density of the mesoscale FAC as a function of (a) the solar wind proton density, (b) dynamic pressure, (c) solar wind velocity, and (d) IMF B_z . The red and gray dots represent positive and negative IMF B_z conditions, respectively. The solid black dots represent the mean values, and the error bars are \pm one standard deviation.

in an upward direction. Each of the red (gray) dots represents the averaged current density of the mesoscale FACs for one event from SW-C under a positive (negative) B_z condition. The mean value for a given range in the horizontal axis is also plotted as a black dot together with the error bar. Except for Figure 9c, we set up the range in such a manner that it can become wide for large values.

Figures 9a–9d indicate that the distributions of the current density of the upward and downward FACs have quite similar tendencies for each of the four parameters, which suggests that the upward and downward FACs are generated through a common generation mechanism. As shown in Figure 9a, the current density tends to increase with the solar wind proton density. A similar tendency can be found in the plot for the solar wind dynamic pressure (Figure 9b). There is no apparent relation between the solar wind velocity and current density (Figure 9c). Because the solar wind dynamic pressure consists of the solar wind proton density and the solar wind velocity, the above-mentioned tendencies indicate that the solar wind proton density is a parameter controlling the current density. Concerning the IMF B_z (Figure 9d), the current density tends to increase in the range of positive IMF B_z . The reason why the solar wind proton density and the IMF B_z are related to the current density will be discussed in Section 4.1. For Figure 9a, we note that the event having an extremely large proton density, that is, approximately 41 cm^{-3} (event on 12:38 UT February 2, 2016) does not have a very large current intensity. The IMF B_z was not positive, that is, the value was approximately -1.2 nT for this event.

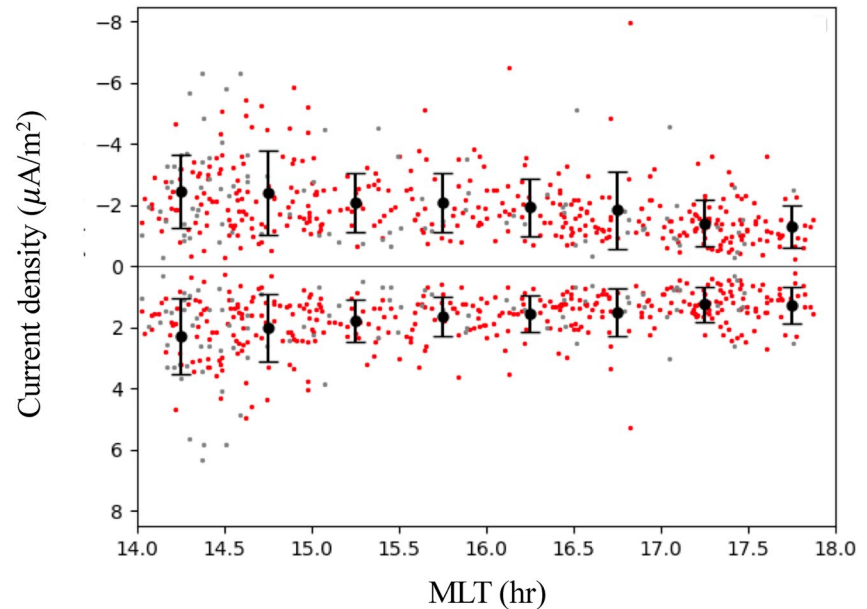


Figure 10. Scatter plot of the current density of the upward/downward FACs as a function of the MLT. The red and gray dots represent positive and negative IMF B_z conditions, respectively. The solid black dots represent the mean values, and the error bars are \pm one standard deviation.

Figure 10 shows the distributions of the current density of the mesoscale FACs against the MLT. The MLT locations used here represent the middle point between P and M . The mesoscale FAC events can occur at any place between this MLT range, and there appears to be a modest tendency for the current density to decrease as the MLT is later for both upward and downward FACs.

4. Discussion

4.1. Generation of the FAC in LLBL During the Northward IMF Condition

Our statistical analyses revealed that the duskside quasistatic mesoscale FAC event could occur in a wide range of solar zenith angles. In other words, the event can occur in the solar-illuminated ionosphere as well as in the dark ionosphere. The results of the statistical analyses also show that the event can be detected at a ratio of more than 20%, that is, approximately once in five times when the IMF B_z is greater than 2 nT. Considering the result from an earlier study by Yokoyama et al. (2020), which has shown that the longitudinal size of the strong upward FAC region, as inferred from the aurora data, is approximately 1–1.5 MLT (for example, their Figures 3h–3j, and Figures 5h–5k), the occurrence ratio of \sim 20%, which is obtained from the survey for the longitudinal range of 4 MLT (from 14 MLT to 18 MLT), implies that the mesoscale FACs much more frequently occur than that ratio when the IMF B_z is greater than 2 nT.

These results consolidate the interpretation by Yokoyama et al. (2020), which states that several pairs of FACs are generated in the duskside LLBL through a mechanism related to physical processes that can be more easily attained as the northward component of IMF increases. As was stated in Introduction, previous studies by satellite observations showed that cold dense ions exist in the LLBL during the prolonged northward IMF. Yokoyama et al. (2020) interpreted the mesoscale multiple duskside FAC event as being generated in the region where the cold dense ions originating from the magnetosheath are significantly decelerated in the LLBL. A pair of FACs is generated when deceleration occurs in the region where the gradient of the magnetic field exists (see Figure 10c in Yokoyama et al., 2020), as is expressed in the following equation (Strangeway, 2012):

$$(\mathbf{B} \cdot \nabla) \left(\frac{\mathbf{j} \cdot \mathbf{B}}{B^2} \right) = \frac{2\mathbf{B}}{B^2} \cdot \left(\rho \frac{D\mathbf{u}}{Dt} \times \frac{\nabla \mathbf{B}}{B} \right), \quad (1)$$

where \mathbf{B} , \mathbf{j} , ρ , D/Dt , and \mathbf{u} are the magnetic field, current density, plasma mass density, total time derivative, and bulk velocity, respectively. Note that on the right-hand side of Equation 1 the pressure-gradient term and the term related to vorticity have been dropped. As was shown in Yokoyama et al. (2020), the pressure gradient does not produce the field-aligned current in the configuration that we assumed. The left-hand part of Equation 1 is the field-aligned gradient of the current density per unit magnetic flux. Its positive (or negative) value represents the FAC flowing away from (or into) the source region in the magnetosphere, that is, a downward (or upward) FAC in the ionosphere. The right-hand part of Equation 1 takes a larger value as the plasma mass density ρ becomes larger. It is expected that the mass density of the ions in the LLBL increases when the solar wind proton density increases. The gradient of the magnetic field would be large as the plasma pressure in the central part of the source region is high, which means that high number density of the ions in the source region may also make the right-hand part of Equation 1 large through the gradient B . The dependence of the FAC density on the solar wind proton density (Figure 9a) is thus reasonable, although the relation between the deceleration of the flow and the number density of the ions is not clear. Similarly, the MLT dependence of the FAC density (Figure 10) is reasonable because the mass density of the ions in the current source region, which come from the magnetosheath, may tend to be smaller as that occurs at a more downstream location. An estimation of the possible deceleration will be given in Section 4.2.

The manner in which the ions enter the closed LLBL from the magnetosheath during the northward IMF has been studied extensively (Fairfield et al., 2000; Fujimoto et al., 1998; Hasegawa, Fujimoto, Phan, et al., 2004; Hasegawa, Fujimoto, Saito, & Mukai, 2004; Nykyri & Otto, 2001; Otto & Fairfield, 2000; Terasawa et al., 1997). Two-dimensional magnetohydrodynamic (MHD) simulations for the boundary layer of the northward IMF by Otto and Fairfield (2000) and Nykyri and Otto (2001) have shown that the vortex motion of KH waves can generate a strongly twisted magnetic field, and that reconnection occurs inside the vortices. Regardless of the occurrence of reconnection inside the vortices, the KH waves tend to occur more often during northward IMF than southward IMF (e.g., Kavosi & Raeder, 2015). Merkin et al. (2013) suggested that plasma compressibility plays a role in the development of KH instability in three-dimensional MHD simulations. A case study based on data from four Cluster satellites provided evidence of direct signatures of local reconnection, where a current sheet with magnetic shear of $\sim 60^\circ$ is formed at the trailing edges of the vortices (Hasegawa et al., 2009). Further evidence on reconnection due to KH waves has been provided by the analyses of the high-resolution data on board the four magnetospheric multiscale spacecraft (Eriksson et al., 2016; Li et al., 2016). If reconnected open field lines are reconnected again, as has been suggested by the three-dimensional simulations by Borgogno et al. (2015), a tailward flow region threaded by the closed magnetic field lines would emerge, and the cold dense ions originating from the magnetosheath would exist in that region. The tailward flow that is formed in the LLBL may have a higher speed as the magnitude of the IMF increases, because the flow is produced by reconnection. Consequently, the IMF B_z dependence on current density (Figure 9d) is reasonable, although our understanding of how the tailward flow decelerates remains lacking.

Reconnection at the high-latitude lobe magnetopause in both the northern and southern hemispheres can form LLBL on the closed field lines under the northward IMF (Onsager et al., 2001; Song & Russell, 1992). This formation would be more effective near the subsolar region than on the flank. As implied by Yokoyama et al. (2020), the source of the mesoscale FACs may lie in the LLBL downstream of $X_{\text{GSM}} = -30 R_E$, which is far from the subsolar region. The double-lobe reconnection is not responsible for the generation of the mesoscale FACs addressed herein.

4.2. Estimation of the Deceleration of Tailward Flow

The flow deceleration for the generation of the mesoscale FACs can be estimated by using Equation 1. From magnetic flux conservation and current continuity,

$$B_i S_i = B_m S_m, \quad (2)$$

$$\dot{J}_{\parallel i} S_i = \dot{J}_{\parallel m} S_m, \quad (3)$$

where B , $j_{\parallel i}$, and S are the magnetic field, the FAC density, and the transverse area, and subscript “ m ” and “ i ” denote the magnetosphere and the ionosphere, respectively. By using Equations 2 and 3, the current density in the magnetosphere can be written as

$$j_{\parallel m} = j_{\parallel i} \frac{B_m}{B_i}. \quad (4)$$

Taking $j_{\parallel i} \sim 2 \mu\text{A} / \text{m}^2$, $B_m \sim 10 \text{ nT}$, and $B_i \sim 50000 \text{ nT}$, we can get $j_m = 4 \times 10^{-4} \mu\text{A} / \text{m}^2$. Assuming that the generation of the mesoscale FACs occurs at the vicinity of the magnetospheric equatorial plane, the magnetic field in the source region is nearly northward, and the left-hand part of Equation 1 gives

$$(\mathbf{B} \cdot \nabla) \left(\frac{\mathbf{j} \cdot \mathbf{B}}{B^2} \right) = \left(B_z \frac{\partial}{\partial z} \right) \left(\frac{j_{\parallel m}}{B_m} \right) \sim \frac{j_{\parallel m}}{L_z}, \quad (5)$$

where L_z represents the scale of a given region where the magnetic field can be regarded as being northward.

We also consider a cold dense ion region where the horizontal gradient of the northward magnetic field exists. We assume that the plasma flows along the X -axis, and Y -axis is assumed to be perpendicular to X -axis in the same plane. Assuming the steady flow, the right-hand part of Equation 1 becomes

$$\frac{2\mathbf{B}}{B^2} \cdot \left(\rho \frac{D\mathbf{u}}{Dt} \times \frac{\nabla \mathbf{B}}{B} \right) \sim \frac{2\rho}{B_m^2} \left(u_x \frac{\delta u_x}{L_x} \frac{\delta B_z}{L_y} \right), \quad (6)$$

where L_x , L_y , and δB_z are the dimension of the region in the X direction, and the dimension of the region in the Y direction, and the difference of the northward magnetic field in the Y dimension, respectively.

Thus, from Equations 5 and 6, the deceleration of the flow can be written as

$$\delta u_x \sim \left(\frac{j_{\parallel m}}{L_z} \right) \frac{B_m^2}{2\rho} \frac{L_y}{\delta B_z} \frac{L_x}{u_x}. \quad (7)$$

The ratio of the horizontal size in the magnetosphere to that in the ionosphere can be estimated as follows:

$$\frac{L_m}{L_i} = \sqrt{\frac{S_m}{S_i}} = \sqrt{\frac{B_i}{B_m}} \sim 70, \quad (8)$$

where L_m and L_i are the transverse length in the magnetosphere and that in the ionosphere, respectively. The transverse length of the generation region of the mesoscale FAC in the magnetosphere can be obtained by multiplying the transverse length of the mesoscale currents in the ionosphere by this ratio. As shown in Figure 6, the typical latitudinal length of the mesoscale FACs is around 20–30 km. We take $L_y = 30 \times 70 \sim 2000 \text{ km}$, and assume $L_x \sim L_z$ for simplicity.

When we take $\rho \sim 5 \times 10^6 \times 1.67 \times 10^{-27} \text{ kg m}^{-3}$, and assume $\delta B_z = 5 \text{ nT}$, and $u_x = 100 \text{ km s}^{-1}$, flow deceleration δu_x can be estimated to be $\sim 10 \text{ km s}^{-1}$. Thus, roughly 10 km s^{-1} decrease from 100 km s^{-1} may explain the generation of the mesoscale FACs. We note, however, that this estimate is based on the assumption that $L_x \sim L_z$.

4.3. Low Ionospheric Conductivity as an Additional Factor

As shown in Figure 7, the occurrence ratio of the event is somewhat higher in the dark ionosphere than in the sunlit ionosphere. As shown in Figure 5 herein, and in Figure 6b of Yokoyama et al. (2020), the mesoscale upward FAC regions have electron precipitation whose energy fluxes are relatively large. This suggests that as a larger energy flux of the electron precipitation occurs, the mesoscale upward FAC can increase its intensity such that Condition 2 for event identification (Section 3.1) may be easier to satisfy.

Regarding the tendency of the energy flux of the electron precipitation to be larger in the dark ionosphere than in the sunlit ionosphere, several previous studies have indicated its significance (Liou et al., 2001; Newell et al., 1996; Shue et al., 2001). A possible mechanism that can explain this tendency, in particular, the preferred occurrence of discrete auroral arcs for low ionospheric conductivity, is the ionospheric feedback instability (Atkinson, 1970; Lysak, 1991; Sato, 1978). This mechanism requires a change in the

electron density in the ionosphere, which causes variations in the Pedersen and Hall conductivities. The ionospheric feedback instability, which is operative along the field lines where the duskside mesoscale FACs occur, is qualitatively consistent with the result, exhibiting a somewhat higher ratio in the dark ionosphere. However, we note that the ionospheric electron density variation, which is responsible for the ionospheric feedback instability, is not very prominent, as can be inferred from the DMSP electron precipitation data (Figure 5 herein, and Figure 6b of Yokoyama et al. (2020)) because the energy of the electron precipitation is a few hundred electron volts at the most.

5. Conclusions

By analyzing the magnetic field data obtained by Swarm satellites for a period of more than three years, we examined the quasistatic mesoscale multiple FACs embedded in the duskside diminished Region 1/2 current system. These FAC events were identified in 577 orbits that passed through the high-latitude part of the 14–18 MLT auroral oval. The results of our statistical analyses based on these events can be summarized as follows:

1. The mesoscale FAC events consist of multiple upward and downward FACs, and the latitudinal size of the upward FAC regions does not usually exceed 40 km. This generally agrees with our earlier result from the event study, showing that the typical latitudinal size of the mesoscale upward FACs is 20–30 km (Yokoyama et al., 2020).
2. The occurrence ratio of the FAC events is less than 10% for an IMF B_z of <1 nT. As B_z increases, so does the occurrence ratio. For B_z greater than 2 nT, the event can be detected at a ratio of more than 20%. Considering the possible longitudinal size, we can infer from this ratio that the events are almost always present somewhere in the duskside auroral oval when the IMF has a northward component. This provides conclusive evidence demonstrating that the quasistatic mesoscale FACs in the duskside sector are pertinent to a northward IMF condition, and that they are not a simple remnant of the diminished Region 1.
3. The density of the FACs tends to increase with that of the solar wind proton density. The solar wind proton density is a controlling parameter for the FAC density. IMF B_z also appears to be related for the current density.
4. The FAC events can occur in a wide range of solar zenith angles, that is, 65–135°, indicating that whether the ionosphere is sunlit or dark is not crucial for the appearance of the event. It appears that the ionospheric conductivity is not very important for the generation of the event.
5. These results consolidate the interpretation by Yokoyama et al. (2020), which states that several pairs of FACs are generated in the duskside LLBL through a mechanism related to the solar wind plasma entry processes that can be more easily attained as the northward component of the IMF increases. Although the present analysis cannot determine the physical processes unambiguously, a probable explanation is the phenomenon of reconnection inside the vortices of the KH waves.

Data Availability Statement

Swarm magnetometer data used in this study are provided under the ESA Swarm Science and Validation Opportunity project (ID:10230) and available at <https://earth.esa.int/>. OMNI solar wind data were obtained through NASA/CDAWeb (<http://cdaweb.sci.gsfc.nasa.gov/index.html>).

Acknowledgments

The authors wish to thank K. Hosokawa for helpful discussions. The work by S. Taguchi is supported by the Kyoto University Foundation, and ISHIZUE 2019 of Kyoto University Research Development Program. The work by T. Iyemori is supported by JSPS KAKENHI Grant Number 15H05815 and 25287128.

References

- Araki, T., Kamei, T., & Iyemori, T. (1984). Polar cap vertical currents associated with northward interplanetary magnetic field. *Geophysical Research Letters*, *11*(1), 23–26. <https://doi.org/10.1029/gl011i001p00023>
- Atkinson, G. (1970). Auroral arcs: Result of the interaction of a dynamic magnetosphere with the ionosphere. *Journal of Geophysical Research*, *75*, 4746–4755. <https://doi.org/10.1029/ja075i025p04746>
- Borgogno, D., Califano, F., Faganello, M., & Pegoraro, F. (2015). Double-reconnected magnetic structures driven by Kelvin-Helmholtz vortices at the earth's magnetosphere. *Journal Physics of Plasmas*, *22*(3), 032301. <https://doi.org/10.1063/1.4913578>
- Carter, J. A., Milan, S. E., Fogg, A. R., Sangha, H., Lester, M., Paxton, L. J., & Anderson, B. J. (2020). The evolution of long-duration cusp spot emission during lobe reconnection with respect to field-aligned currents. *Journal of Geophysical Research: Space Physics*, *125*, e2020JA027922. <https://doi.org/10.1029/2020ja027922>

- Eriksson, S., Lavraud, B., Wilder, F. D., Stawarz, J. E., Giles, B. L., Burch, J. L., et al. (2016). Magnetospheric multiscale observations of magnetic reconnection associated with Kelvin-Helmholtz waves. *Geophysical Research Letters*, *43*, 5606–5615. <https://doi.org/10.1002/2016GL068783>
- Fairfield, D. H., Otto, A., Mukai, T., Kokubun, S., Lepping, R. P., Steinberg, J. T., et al. (2000). Geotail observations of the Kelvin-Helmholtz instability at the equatorial magnetotail boundary for parallel northward fields. *Journal of Geophysical Research*, *105*, 21159–21173. <https://doi.org/10.1029/1999ja000316>
- Friis-Christensen, E., Lühr, H., & Hulot, G. (2006). SW-A constellation to study the earth's magnetic field. *Earth Planets and Space*, *58*(4), 351–358. <https://doi.org/10.1186/BF03351933>
- Fujimoto, M., Terasawa, T., Mukai, T., Saito, Y., Yamamoto, T., & Kokubun, S. (1998). Plasma entry from the flanks of the near-earth magnetotail: Geotail observations. *Journal of Geophysical Research*, *103*(A3), 4391–4408. <https://doi.org/10.1029/97JA03340>
- Gjerloev, J. W., Ohtani, S., Iijima, T., Anderson, B., Slavin, J., & Le, G. (2011). Characteristics of the terrestrial field-aligned current system. *Annales Geophysicae*, *29*(19), 1713–1729. <https://doi.org/10.5194/angeo-29-1713-2011>
- Hasegawa, H., Fujimoto, M., Phan, T., Rème, H., Balogh, A., Dunlop, M. W., et al. (2004). Transport of solar wind into earth's magnetosphere through rolled-up Kelvin-Helmholtz vortices. *Nature*, *430*, 755–758. <https://doi.org/10.1038/nature02799>
- Hasegawa, H., Fujimoto, M., Saito, Y., & Mukai, T. (2004). Dense and stagnant ions in the low-latitude boundary region under northward interplanetary magnetic field. *Geophysical Research Letters*, *31*, L06802. <https://doi.org/10.1029/2003gl019120>
- Hasegawa, H., Retinò, A., Vaivads, A., Khotyaintsev, Y., André, M., Nakamura, T. K. M., et al. (2009). Kelvin-Helmholtz waves at the earth's magnetopause: Multiscale development and associated reconnection. *Journal of Geophysical Research*, *114*, A12207. <https://doi.org/10.1029/2009JA014042>
- Huang, T., Lühr, H., Wang, H., & Xiong, C. (2017). The relationship of high-latitude thermospheric wind with ionospheric horizontal current, as observed by CHAMP satellite. *Journal of Geophysical Research: Space Physics*, *122*, 12378–12392. <https://doi.org/10.1002/2017ja024614>
- Iijima, T., & Potemra, T. A. (1978). Large-scale characteristics of field-aligned currents associated with substorms. *Journal of Geophysical Research*, *83*(A2), 599–615. <https://doi.org/10.1029/JA083iA02p00599>
- Iijima, T., Potemra, T. A., Zanetti, L. J., & Bythrow, P. F. (1984). Large-scale Birkeland currents in the dayside polar region during strongly northward IMF: A new Birkeland current system. *Journal of Geophysical Research*, *89*(A9), 7441–7452. <https://doi.org/10.1029/ja089ia09p07441>
- Kavosi, S., & Raeder, J. (2015). Ubiquity of Kelvin-Helmholtz waves at Earth's magnetopause. *Nature Communications*, *6*(1), 7019. <https://doi.org/10.1038/ncomms8019>
- Li, W., André, M., Khotyaintsev, Y. V., Vaivads, A., Graham, D. B., Toledo-Redondo, S., et al. (2016). Kinetic evidence of magnetic reconnection due to Kelvin-Helmholtz waves. *Geophysical Research Letters*, *43*, 5635–5643. <https://doi.org/10.1002/2016GL069192>
- Liou, K., Newell, P. T., & Meng, C. -I. (2001). Seasonal effects on auroral particle acceleration and precipitation. *Journal of Geophysical Research*, *106*(A4), 5531–5542. <https://doi.org/10.1029/1999JA000391>
- Lühr, H., Park, J., Gjerloev, J. W., Rauberg, J., Michaelis, I., Merayo, J. M. G., & Brauer, P. (2015). Field-aligned currents' scale analysis performed with the swarm constellation. *Geophysical Research Letters*, *42*(1), 1–8. <https://doi.org/10.1002/2014GL062453>
- Lysak, R. L. (1991). Feedback instability of the ionospheric resonant cavity. *Journal of Geophysical Research*, *96*(A2), 1553–1568. <https://doi.org/10.1029/90JA02154>
- Merkin, V. G., Lyon, J. G., & Claudepierre, S. G. (2013). Kelvin-Helmholtz instability of the magnetospheric boundary in a three-dimensional global MHD simulation during northward IMF conditions. *Journal of Geophysical Research - A: Space Physics*, *118*, 5478–5496. <https://doi.org/10.1002/jgra.50520>
- Newell, P. T., Meng, C.-I., & Lyons, K. M. (1996). Suppression of discrete aurora by sunlight. *Nature*, *381*, 766–767. <https://doi.org/10.1038/381766a0>
- Nykyri, K., & Otto, A. (2001). Plasma transport at the magnetospheric boundary due to reconnection in Kelvin-Helmholtz vortices. *Geophysical Research Letters*, *28*, 3565–3568. <https://doi.org/10.1029/2001gl013239>
- Olsen, N., Friis-Christensen, E., Floberghagen, R., Alken, P., Beggan, C. D., Chulliat, A., et al. (2013). The swarm satellite constellation application and research facility (SCARF) and swarm data products. *Earth Planets and Space*, *65*, 1–1200. <https://doi.org/10.5047/eps.2013.07.001>
- Onsager, T. G., Scudder, J. D., Lockwood, M., & Russell, C. T. (2001). Reconnection at the high-latitude magnetopause during northward interplanetary magnetic field conditions. *Journal of Geophysical Research*, *106*(A11), 25467–25488. <https://doi.org/10.1029/2000JA000444>
- Otto, A., & Fairfield, D. H. (2000). Kelvin-Helmholtz instability at the magnetotail boundary: MHD simulation and comparison with geotail observations. *Journal of Geophysical Research*, *105*, 21175–21190. <https://doi.org/10.1029/1999ja000312>
- Rich, F. J., & Gussenhoven, M. S. (1987). The absence of region 1/Region 2 field-aligned current during prolonged quiet times. *Geophysical Research Letters*, *14*(7), 689–692. <https://doi.org/10.1029/gl014i007p00689>
- Ritter, P., Lühr, H., & Rauberg, J. (2013). Determining field-aligned currents with the swarm constellation mission. *Earth Planets and Space*, *65*, 9. <https://doi.org/10.5047/eps.2013.09.006>
- Sato, T. (1978). A theory of quiet auroral arcs. *Journal of Geophysical Research*, *83*(A3), 1042–1048. <https://doi.org/10.1029/JA083iA03p01042>
- Shue, J.-H., Newell, P. T., Liou, K., & Meng, C. -I. (2001). The quantitative relationship between auroral brightness and solar EUV Pedersen conductance. *Journal of Geophysical Research*, *106*(A4), 5883–5894. <https://doi.org/10.1029/2000JA003002>
- Song, P., & Russell, C. T. (1992). Model of the formation of the low-latitude boundary-layer for strongly northward interplanetary magnetic-field. *Journal of Geophysical Research*, *97*, 1411–1420. <https://doi.org/10.1029/91ja02377>
- Strangeway, R. J. (2012). The relationship between magnetospheric processes and Auroral field-aligned current morphology. In A. Keil-ing, E. Donovan, F. Bagenal, & T. Karlsson (Eds.), *Auroral phenomenology and magnetospheric processes: Earth and other planets* (pp. 355–364). <https://doi.org/10.1029/2012GM001211>
- Taguchi, S., Hosokawa, K., Ogawa, Y., Aoki, T., & Taguchi, M. (2012). Double bursts inside a poleward-moving auroral form in the cusp. *Journal of Geophysical Research*, *117*, A12301. <https://doi.org/10.1029/2012ja018150>
- Taguchi, S., Sugiura, M., Winningham, J. D., & Slavin, J. A. (1993). Characterization of the IMF B_y -dependent field-aligned currents in the cleft region based on DE 2 observations. *Journal of Geophysical Research*, *98*(A2), 1393–1407. <https://doi.org/10.1029/92JA01014>
- Taguchi, S., Tawara, A., Hairston, M. R., Slavin, J. A., Le, G., Matzka, J., & Stolle, C. (2015). Response of reverse convection to fast IMF transitions. *Journal of Geophysical Research: Space Physics*, *120*, 4020–4037. <https://doi.org/10.1002/2015ja021002>
- Terasawa, T., Fujimoto, M., Mukai, T., Saito, Y., Yamamoto, T., Machida, S., et al. (1997). Solar wind control of density and temperature in the near-Earth plasma sheet: WIND-GEOTAIL collaboration. *Geophysical Research Letters*, *24*, 935–938. <https://doi.org/10.1029/96GL04018>

- Thébault, E., Finlay, C., Beggan, C. D., Alken, P., Aubert, J., Barrois, O., et al. (2015). International geomagnetic reference field: The 12th generation. *Earth Planets and Space*, *67*, 79. <https://doi.org/10.1186/s40623-015-0228-9>
- Vennerstrøm, S., Moretto, T., Olsen, N., Friis-Christensen, E., Stampe, A. M., & Watermann, J. F. (2002). Field-aligned currents in the day-side cusp and polar cap region during northward IMF. *Journal of Geophysical Research*, *107*(A8). <https://doi.org/10.1029/2001JA009162>
- Wing, S., Ohtani, S., Newell, P. T., Higuchi, T., Ueno, G., & Weygand, J. M. (2010). Dayside field-aligned current source regions. *Journal of Geophysical Research*, *115*, A12215. <https://doi.org/10.1029/2010JA015837>
- Xiong, C., & Lühr, H. (2014). An empirical model of the auroral oval derived from CHAMP field-aligned current signatures—Part 2. *Annales Geophysicae*, *32*, 623–631. <https://doi.org/10.5194/angeo-32-623-2014>
- Yokoyama, Y., Taguchi, S., Iyemori, T., & Hosokawa, K. (2020). The quasi-persistent feature of highly structured field-aligned currents in the duskside auroral oval: Conjugate observation via Swarm satellites and a ground all-sky imager. *Journal of Geophysical Research: Space Physics*, *125*, e2019JA027594. <https://doi.org/10.1029/2019JA027594>